

<https://doi.org/10.1038/s41612-024-00707-0>

Changes to tropical cyclone trajectories in Southeast Asia under a warming climate

Andra J. Garner¹ ✉, Dhruvajyoti Samanta², Mackenzie M. Weaver³ & Benjamin P. Horton^{2,4}

The impacts of tropical cyclones (TCs) on Southeast Asia's coastlines are acute due to high population densities in low-lying coastal environments. However, the trajectories of TCs are uncertain in a warming climate. Here, we assess >64,000 simulated TCs from the nineteenth century to the end of the twenty-first century for both moderate- and high-emissions scenarios. Results suggest changes to TC trajectories in Southeast Asia, including: (1) poleward shifts in both genesis and peak intensification rates; (2) TC formation and fastest intensification closer to many coastlines; (3) increased likelihoods of TCs moving most slowly over mainland Southeast Asia; and (4) TC tracks persisting longer over land. In the cities of Hai Phong (Vietnam), Yangon (Myanmar), and Bangkok (Thailand), these variations result in future increases in both peak TC intensity and TC duration compared to historical TCs.

Climate change poses an existential threat to Southeast Asian nations^{1–6}. Coastal hazards in a warming climate are particularly concerning for the region, which is home to more than 70% of the total global population currently living on land that is exposed to future sea-level rise^{1,2,7} (Fig. 1). Tropical cyclones (TCs) are amongst the most damaging and costly coastal hazards in many locations^{8–10}, creating concerning vulnerabilities for many of Southeast Asia's coastal communities^{1,2,11–14}. Understanding how a warming climate may impact the trajectories of TCs is critical to comprehending how coastal hazards in Southeast Asia may evolve in the future¹⁵.

In a warming climate, TCs may be more intense^{1,9–11,13}, because they serve as a natural physical mechanism to transport excess heat from the tropics to more poleward regions¹⁶. However, to fully comprehend how the TC hazard in Southeast Asia may change in a warming climate, we must also understand variations in TC trajectories and storm characteristics along those trajectories^{17–20}. For example, previous studies have suggested an expansion of the Hadley cell due to anthropogenic warming (especially in the Northwest Pacific), which could contribute to TCs forming and intensifying at more poleward latitudes^{18,21,22}. Other studies suggest that in recent decades, TCs in the Northwest Pacific have traveled farther north and persisted longer, leading to more frequent TC impacts for Korea and Japan in September²³. Another study indicates a shift in TC trajectories that causes more TCs to travel near the Ayeyarwady Delta coast in Myanmar, a low-lying coastal region known for rice production²⁴.

Given the vital role of TC trajectories in determining the hazards Southeast Asian coastlines face from TCs both now and in the future, we must establish an improved understanding of how modern tracks in the region have changed from historical norms, as well as how future tracks may

further evolve. Here, we use >64,000 TCs downscaled from an ensemble of nine Coupled Model Intercomparison Project Phase 6 (CMIP6) models for historical, modern, moderate- (Shared Socioeconomic Pathway [SSP]2-4.5), and high-emissions future (SSP5-8.5) scenarios to understand changes to the TC tracks that impact Southeast Asia. We consider changes to locations where TCs form, TC track characteristics (including maximum intensification rates and minimum translation speeds), and locations where TCs terminate. We evaluate the implications of these changes to TC tracks for two of Southeast Asia's megacities (Yangon, Myanmar, and Bangkok, Thailand) as well as the major Red River Delta port city of Hai Phong, Vietnam, all of which are particularly susceptible to TC hazards.

Results

We use nine CMIP6 models²⁵ to evaluate how the track characteristics of TCs that impact Southeast Asia change from a historical era (1881–1900) to a modern era (1981–2000) to a future era (2081–2100) for both moderate (SSP2-4.5)²⁶ and high emissions (SSP5-8.5)²⁶. TC track datasets include 16,200 downscaled storms for each era to robustly assess changes to track characteristics. Additional details, including caveats specific to CMIP6 model selection and the downscaling method used here, are included in the “Methods”.

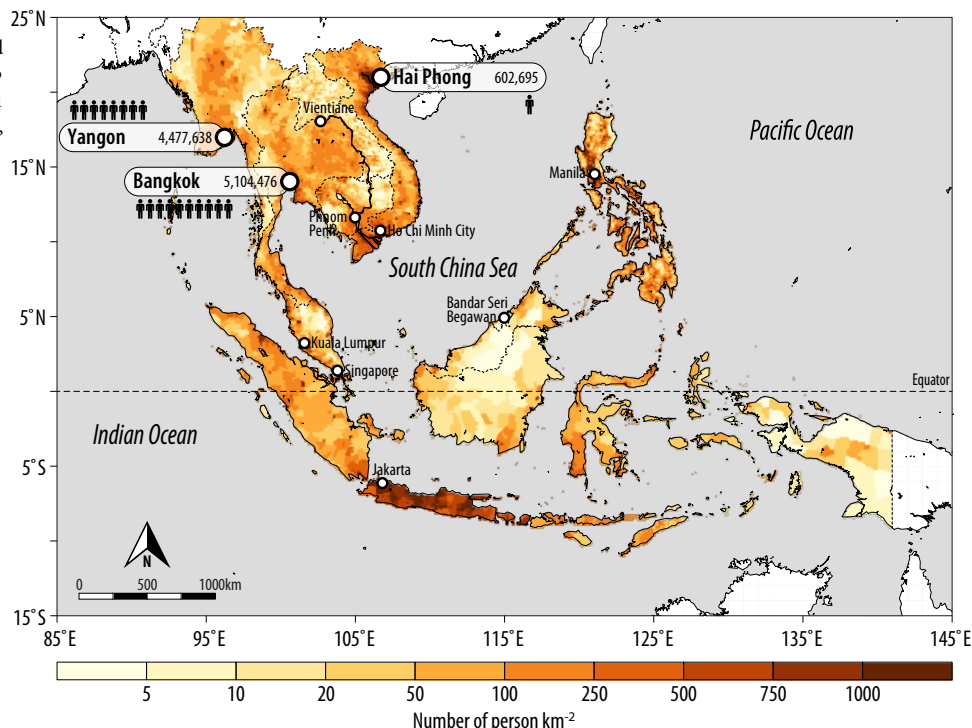
To compare regional trends across time, we focus our analyses for each characteristic on distinct regions within and around Southeast Asia (Table 1).

Tropical cyclone genesis

There are statistically significant (99% credible interval; CI) increases in TC genesis from the historical era to the end of the twenty-first

¹Department of Environmental Science, Rowan University, Glassboro, NJ 08028, USA. ²Earth Observatory of Singapore, Nanyang Technological University, Singapore 639798, Singapore. ³Department of Earth & Environmental Science, University of Pennsylvania, Philadelphia, PA 19104, USA. ⁴Asian School of the Environment, Nanyang Technological University, Singapore 639798, Singapore. ✉ e-mail: gamera@rowan.edu

Fig. 1 | Regional map and population density. Map showing the Southeast Asia region and gridded population density (unit: person km⁻²) estimates based on NASA’s Gridded Population of the World Dataset (updated in 2020). Also shown on the map are populations for points of interest including Hai Phong, Vietnam; Yangon, Myanmar; and Bangkok, Thailand.



century in the northern Northwest Pacific, the South China Sea, and the Bay of Bengal (Fig. 2 and Table 1). In a high-emissions future, genesis becomes >20% more common in the northern Northwest Pacific, South China Sea, and Bay of Bengal compared to the historical era (Table 1; see “Methods”). Alternatively, there is a decrease in TC genesis from the historical era to the end of the twenty-first century in a more southerly portion of the Northwest Pacific (east of the Philippines) under both moderate- and high-emissions futures (Fig. 2 and Supplementary Fig. 1)

Location and magnitude of tropical cyclone maximum intensification rates

Analyses of the locations along TC tracks where the largest 2-h increase in maximum wind speed occurs reveal statistically significant increases (99% CI) in the likelihood of TCs intensifying most quickly in the northern Northwest Pacific, South China Sea, and Bay of Bengal (Supplementary Fig. 2 and Fig. 3A–F) from the historical era to the end of the twenty-first century. In a high-emissions future, TC maximum intensification rates become more common in the northern Northwest Pacific (~19%), South China Sea (~13%), and Bay of Bengal (~39%) at the end of the twenty-first century relative to the historical era (Table 1). These increases are accompanied by decreases compared to the historical era in the likelihood of TCs intensifying most quickly elsewhere around Southeast Asia, including more southerly regions of the Northwest Pacific, northern portions of the Bay of Bengal, and certain areas in and near the Gulf of Thailand (Fig. 3A–C).

The magnitudes of maximum TC intensification rates also increase over time (Fig. 3G and Supplementary Fig. 3). Across the model ensemble, the greatest increases occur for a high-emissions future. For example, in a high-emissions future, the 83rd percentile of 2-h maximum intensification rates increases by more than 50% compared to the historical era (from 5.8 kts to 9.2 kts; Supplementary Fig. 3). In addition, the exceedance probability of a 10-kt maximum intensification rate across a 2-h window increases from ≤4% in the historical and modern eras to 11.2% in a moderate-emissions future and 14% in a high-emissions future (Fig. 3G).

Slowest minimum translation speed along tropical cyclone trajectories

From the historical era to the future, there are statistically significant (99% CI) increases in the likelihood of TCs traveling most slowly in certain regions, including over mainland Southeast Asia (Fig. 4 and Table 1). At the same time, there is a statistically significant decreased likelihood of TCs moving most slowly near the Philippines from the historical era to the future (Fig. 4 and Table 1). Overall, TC minimum translation speed becomes ~34% more common over mainland Southeast Asia, ~13% more common over the Bay of Bengal, and ~17% less common near the Philippines in a high-emissions future compared to the historical era (Table 1).

Tropical cyclone termination points

Compared to the historical era, there are statistically significant increases (99% CI) in the likelihood of future TCs terminating over mainland Southeast Asia (Fig. 5A–F and Table 1). The greatest increase in mainland Southeast Asia TC termination within the model ensemble occurs for a moderate-emissions future, with termination becoming ~15% more common for the region relative to the historical era (Table 1). Simultaneously, it becomes less likely for TCs to terminate near Japan and along the southeastern coast of China in the future compared to the historical era, though these decreases are not significant for a 99% CI (Fig. 5A–F and Table 1). Over the same period, there are also apparent increases in TC termination in the Bay of Bengal and its surrounding coastlines, at more inland locations in China, and in the northern and eastern portions of the North Pacific Basin, including coastal Siberia, Alaska, and Canada (Fig. 5A–F and Supplementary Fig. 6).

Consistent with increased rates of TC termination over mainland Southeast Asia and inland China from the historical era to the future, results further indicate that future land-terminating TCs tend to persist longer after making landfall than their historical counterparts, regardless of emission scenario (Fig. 5G and Supplementary Fig. 7).

Table 1 | Percentages of TC tracks with given characteristics in each period

		Historical	Modern	Future SSP2–4.5	Future SSP5–8.5
Genesis	Northwest Pacific Lat. Bds: 19°N – 28°N Lon. Bds.: 125°E – 148°E	9.7% (9.1% – 10.3%)	9.0% (8.4% – 9.5%)	10.5% (9.9% – 11.1%) [+8.2%]	12.2% (11.5% – 12.9%) [+25.8%]
	South China Sea Lat. Bds: 15°N – 22°N Lon. Bds.: 106°E – 119.5°E	5.2% (4.8% – 5.6%)	5.5% (5.0% – 5.9%)	6.6% (6.1% – 7.1%) [+26.9%]	7.1% (6.6% – 7.9%) [+36.5%]
	Bay of Bengal Lat. Bds: 11°N – 17°N Lon. Bds.: 80.5°E – 95.5°E	4.4% (4.0% – 4.9%)	4.3% (3.9% – 4.7%)	5.4% (5.0% – 5.9%) [+22.7%]	5.3% (4.9% – 5.8%) [+20.5%]
Maximum intensification	Northwest Pacific Lat. Bds: 19°N – 28°N Lon. Bds.: 125°E – 148°E	13.3% (12.6% – 14.0%)	12.4% (11.7% – 13.1%)	14.3% (13.6% – 15.0%) [+7.5%]	15.8% (15.0% – 16.5%) [+18.8%]
	South China Sea Lat. Bds: 15°N – 22°N Lon. Bds.: 106°E – 119.5°E	7.6% (7.0% – 8.1%)	7.8% (7.2% – 8.3%)	8.8% (8.2% – 9.3%) [+15.8%]	8.6% (8.0% – 9.2%) [+13.2%]
	Bay of Bengal Lat. Bds: 11°N – 17°N Lon. Bds.: 80.5°E – 95.5°E	3.1% (2.8% – 3.5%)	3.3% (2.9% – 3.6%)	4.0% (3.6% – 4.4%) [+29.0%]	4.3% (3.9% – 4.7%) [+38.7%]
Minimum translation speed	Philippines Lat. Bds: 5°N – 19°N Lon. Bds.: 115°E – 129°E	14.7% (14.0% – 15.4%)	14.0% (13.3% – 14.7%)	13.5% (12.8% – 14.2%) [–8.2%]	12.2% (11.6% – 12.9%) [–17.0%]
	Mainland SE Asia Lat. Bds: 10°N – 25°N Lon. Bds.: 96°E – 108°E	3.5% (3.2% – 3.9%)	3.9% (3.5% – 4.3%)	4.7% (4.3% – 5.2%) [+34.3%]	4.7% (4.3% – 5.2%) [+34.3%]
	Bay of Bengal Lat. Bds: 11°N – 17°N Lon. Bds.: 80.5°E – 95.5°E	3.2% (2.9% – 3.6%)	3.2% (2.8% – 3.5%)	3.9% (3.5% – 4.3%) [+21.9%]	3.6% (3.2% – 4.0%) [+12.5%]
Termination	Japan Lat. Bds: 32°N – 47°N Lon. Bds.: 130°E – 146°E	12.8% (12.1% – 13.5%)	12.4% (11.7% – 13.0%)	11.5% (10.9% – 12.1%) [–10.2%]	12.5% (11.8% – 13.1%) [–2.3%]
	Coastal China Lat. Bds: 22°N – 31°N Lon. Bds.: 108.5°E – 122°E	13.8% (13.1% – 14.5%)	12.9% (12.2% – 13.6%)	13.3% (12.6% – 13.9%) [–3.6%]	12.5% (11.8% – 13.2%) [–9.4%]
	Mainland SE Asia Lat. Bds: 10°N – 25°N Lon. Bds.: 96°E – 108°E	14.4% (13.7% – 15.1%)	14.8% (14.1% – 15.6%)	16.6% (15.8% – 17.4%) [+15.3%]	16.4% (15.6% – 17.1%) [+13.9%]

Bootstrapped 99% credible intervals are shown in parentheses; categories align with those shown in parts D–F of Figs. 2–5. The proportional change from historical to future eras in the percentage of TC genesis, maximum intensification, minimum translation speed, and termination in key regions are shown in colored text in brackets in the final two columns.

Peak winds and tropical cyclone duration in Southeast Asian coastal communities

Changing TC track characteristics have important implications for impacts on Southeast Asian communities. Within our model ensemble, the maximum TC wind speeds occurring at Hai Phong (Vietnam), Yangon (Myanmar), and Bangkok (Thailand) become more intense (Fig. 6A–E and Supplementary Figs. 8A–E and 9) from the historical era to the end of the twenty-first century. At all locations, significant increases in the maximum wind speed occur within the risk-determining upper tail of distributions for at least one future emissions scenario (Figs. 6 and S8, S9). The most intense future maximum wind speeds occur at Hai Phong and Yangon, where peak wind speeds approach or exceed 150 kts for future simulations. At Hai Phong, the 99th percentile of peak maximum TC wind speeds increase by up to ~31% relative to historical values (Fig. 6A) for a moderate-emissions future, while at Yangon, the 99th percentile of future maximum TC wind

speeds increase ~48% in a high-emissions future relative to historical values (Fig. 6C). Bangkok has the least intense future maximum wind speeds of all three locations, with most TCs producing maximum wind speeds of 100 kts or less. However, when considering the relative changes from the historical era, Bangkok experiences the steepest increase of all three locations, with the 99th percentile of a future moderate-emissions distribution increasing by >100% compared to historical simulations (Fig. 6E).

Future TCs across the model ensemble also tend to persist longer than their historical counterparts at Hai Phong, Yangon, and Bangkok (Fig. 6B–F and Supplementary Fig. 8D–F). At Hai Phong, there are increases in the distribution means of TC duration, with historical TC impacts lasting an average of 7.9 h, and TCs in a high-emissions future lasting as long as 9.6 h on average (Fig. 6B and Supplementary Fig. 8B). At Yangon, there are increases in both the overall distribution mean and in the duration of the longest-lasting future TCs compared to their historical counterparts,

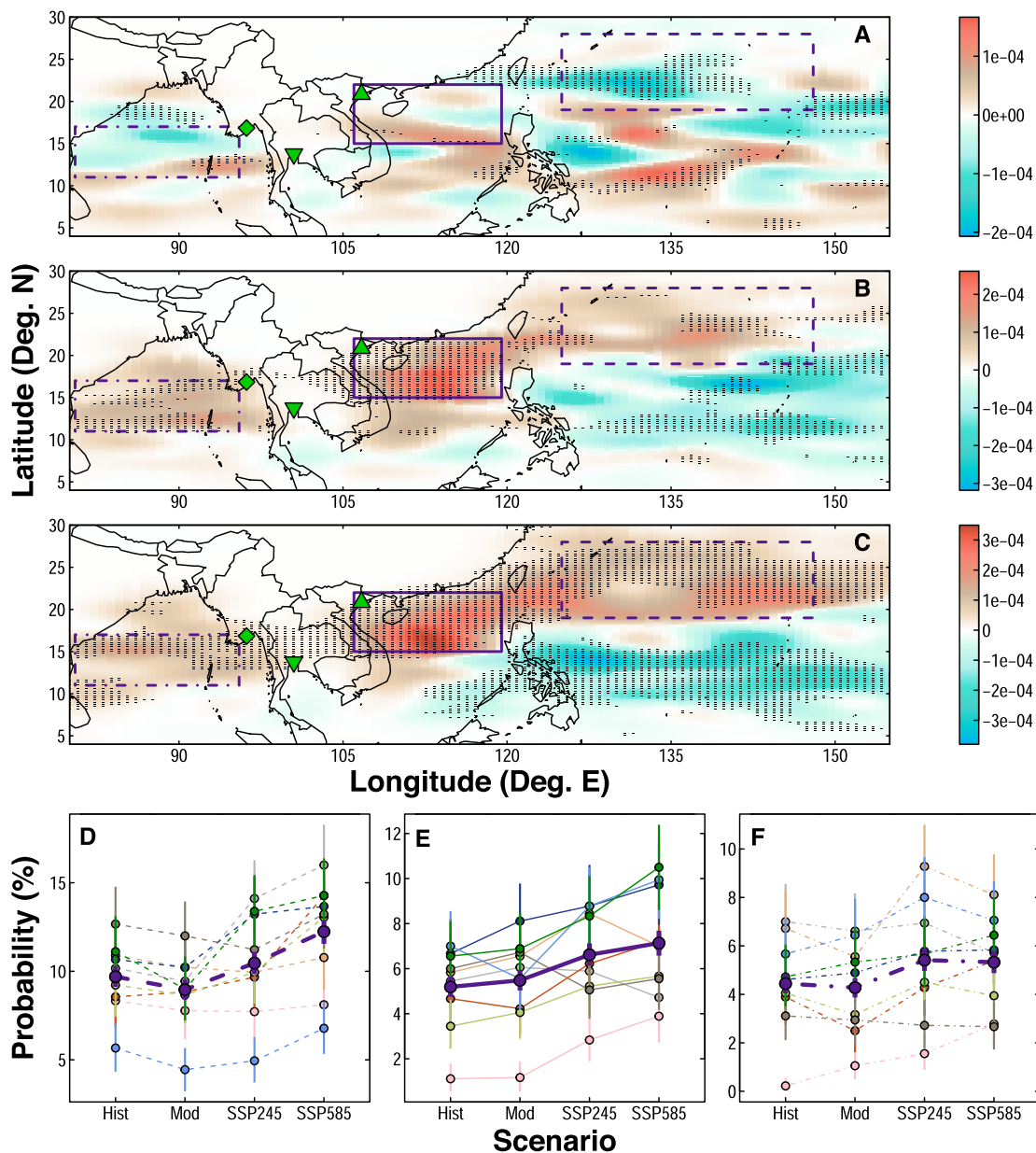


Fig. 2 | Density difference maps and probabilities of TC genesis. Maps portraying the differences in TC genesis density for (A) the modern era (1981–2000) compared to the historical era (1881–1900), (B) a moderate-emissions future (2081–2100; SSP2-4.5) compared to the historical era, and (C) a high-emissions future (2081–2100; SSP5-8.5) compared to the historical era. Rectangles on the maps represent the Northwest Pacific region (dashed rectangle), the South China Sea region (solid rectangle), and the Bay of Bengal region (dot-dash rectangle); green markers on maps indicate the locations of Hai Phong, Vietnam (upwards triangle); Bangkok, Thailand (downwards triangle); and Yangon, Myanmar (diamond). Hatching on maps shows grid cells where at least 7 of the 9 models assessed indicate

the same sign (positive or negative) density difference. The density units shown by map color bars are track points per grid cell. Line plots indicate the probability of TC genesis occurring within the regions outlined by rectangles on the maps, including (D) the Northwest Pacific region, (E) the South China Sea region, and (F) the Bay of Bengal region. Error bars on the line plots show the bootstrapped 99% credible interval. Individual models shown in line plots are: CanESM (gray); CESM (pink); CNRM (orange); ECEarth (red); HadGEM (dark blue); IPSL (light green); MIROC (light blue); MPI (tan); and the UKESM (dark green). The ensemble mean is shown in purple. Note that y-axes in plots (D–F) are varied, to clearly show trends in each region.

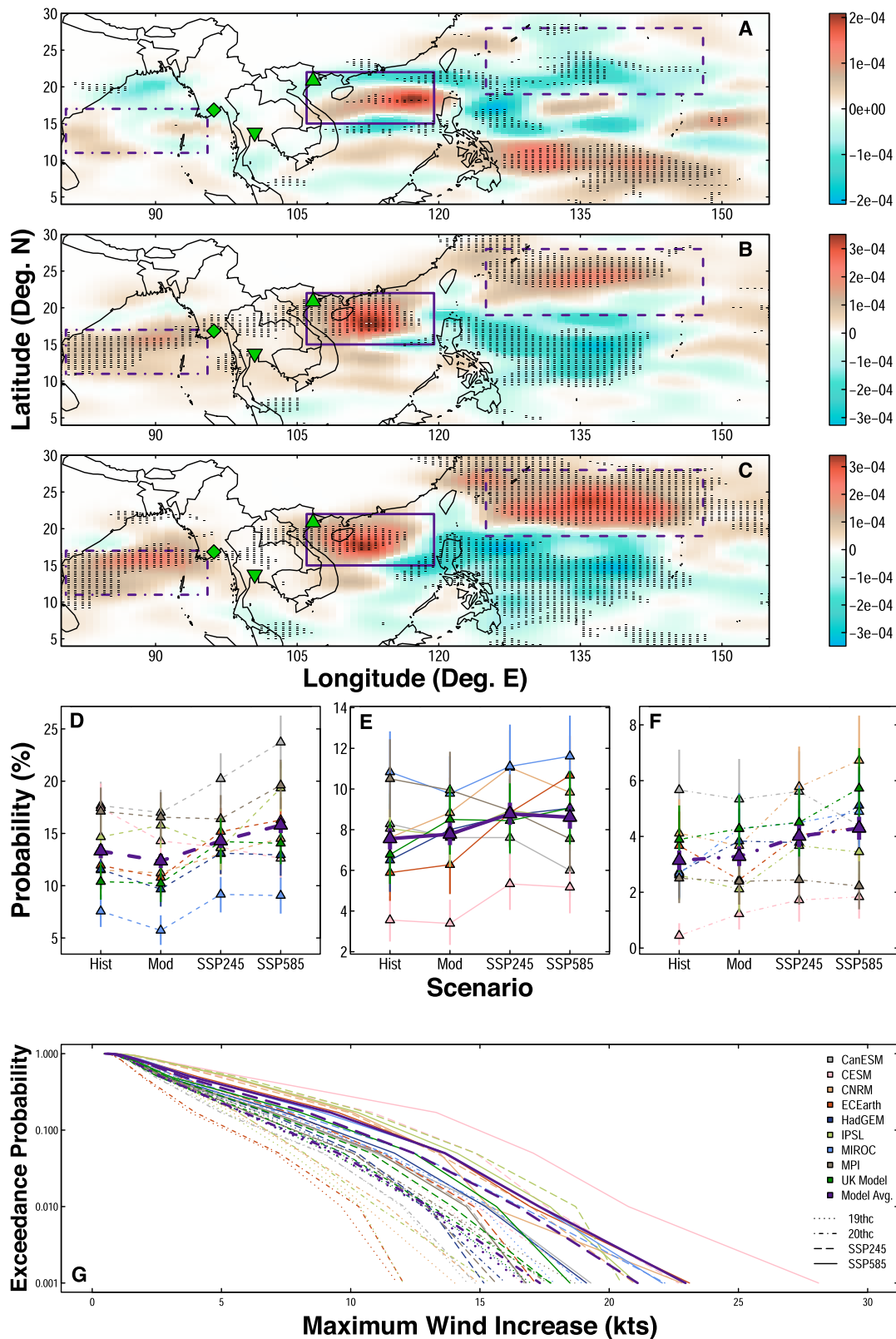
particularly under high emissions (Fig. 6D and Supplementary Fig. 9). Bangkok also exhibits notable increases in TC duration, with a 99th percentile of future TC duration for a moderate-emissions future that is ~72% greater than the equivalent percentile in the historical distribution (Fig. 6F).

Discussion

In a warming climate, changes in the trajectories of TCs that impact Southeast Asia include variations in genesis, maximum intensification rates, minimum translation speeds, and termination. Results presented here aim to quantify these changes and assess their impacts on the TC hazard for key

points of interest in Southeast Asia; however, future work that more fully explores all the climatological drivers that contribute to changing TC trajectories in the region would also be highly beneficial.

Northward shifts in Northwest Pacific TC genesis are consistent with previous studies of both historical records^{18,27,28} and future projections¹⁰, and align well with expected changes due to a poleward expansion of the Hadley cell as the planet warms²⁷. Poleward shifts in future Northwest Pacific genesis (Fig. 2 and Supplementary Fig. 1) are also consistent with similar shifts identified in the Atlantic for a high-emissions future^{17,29}. Within the South China Sea, locations where genesis increases in the future align with



recently observed anomalously warm ocean waters³⁰. Similarly, increases in future TC genesis in the Bay of Bengal are consistent with an increase in historically observed TC genesis in this region due to elevated sea surface temperatures and relative humidity values^{31,32}.

Genesis increases in the Northwest Pacific, South China Sea, and Bay of Bengal are accompanied by increases in TCs also intensifying most quickly

in these regions (Figs. 2 and 3). The simultaneous poleward movement of future genesis and maximum intensification, particularly in the Northwest Pacific, agrees with historical trends^{21,28,33,34}. Increased magnitudes of peak intensification rates also suggest that storms in a warmer future strengthen more quickly than historical TCs (Fig. 3G and Supplementary Fig. 3). For instance, in a high-emissions future, the 83rd percentile maximum

Fig. 3 | Locations where TCs intensify most rapidly. Maps portraying the density differences in TC maximum intensification points for (A) the modern era (1981–2000) compared to the historical era (1881–1900), (B) a moderate-emissions future (2081–2100; SSP2-4.5) compared to the historical era, and (C) a high-emissions future (2081–2100; SSP5-8.5) compared to the historical era. Rectangles on the maps represent the Northwest Pacific region (dashed rectangle), the South China Sea region (solid rectangle), and the Bay of Bengal region (dot-dash rectangle); green markers on maps indicate the locations of Hai Phong, Vietnam (upwards triangle); Bangkok, Thailand (downwards triangle); and Yangon, Myanmar (diamond). Hatching on maps shows grid cells where at least 7 of the 9 models assessed indicate the same sign (positive or negative) for density difference. The

density units shown by map color bars are track points per grid cell. Line plots indicate the probability of TCs intensifying most rapidly within the regions outlined by rectangles on the maps, including (D) the Northwest Pacific region, (E) the South China Sea region, and (F) the Bay of Bengal region. Error bars on the line plots show the bootstrapped 99% credible interval. Note that *y*-axes in plots (D–F) are varied, to clearly show trends in each region. G Survival functions showing exceedance probabilities of lifetime maximum 2-h wind speed increases (kts) and during the historical era (dotted lines), the modern era (dot-dash lines), a moderate-emissions future (dashed lines), and a high-emissions future (solid lines). Colors of individual models and model ensemble for plots (D–G) are shown in the legend of (G).

intensification rate (9.2 kts in 2 h) is nearly the same as the historical 95th percentile maximum intensification rate (9.3 kts in 2 h; Fig. 3G and Supplementary Fig. 3).

Combined shifts in TC genesis and TC maximum intensification rates suggest that, in a warming climate, TCs are more likely to both form and intensify most quickly closer to Southeast Asian coastlines, and that intensification rates are likely to exceed historical norms. These results agree with recent findings from other basins^{17,29,35,36}. Such compound changes signal a growing coastal hazard throughout the region, given the challenges of forecasting rapid intensification, particularly just before landfall³⁷. There is therefore an urgent need for careful planning and adaptation measures that will foster resilient coastlines capable of withstanding such changes in regional TC hazards.

TC hazards facing coastal communities may be further amplified in a warming climate by exceptionally slow-moving TCs, which have the potential to increase damages from extreme rainfall amounts^{10,19,38}, prolonged storm surges^{39,40}, and extended duration of TC-force winds¹⁹. For instance, Typhoon Vamco (Ulysses; 2020) moved very slowly over the Philippines, producing torrential rainfall and major flooding, resulting in the TC being one of the deadliest to occur in the region^{41,42}. In a warming future, the slowest moving TCs appear less likely to impact the Philippines (Fig. 4), but more likely to impact coastlines around the Bay of Bengal, mainland Southeast Asia, and the South China Sea (Fig. 4). Historical studies of variations in TC forward motion in both the Bay of Bengal and the subtropical Northwest Pacific and South China Sea suggest such TC slowdowns for these regions may already be evident as the planet has warmed, largely due to weaker atmospheric circulation patterns^{43,44}. The increased likelihood for future TCs to move most slowly near densely populated regions around Southeast Asia is particularly concerning, given that TC-related floods have proven to be especially damaging for the region⁴⁵.

Although some decreases in the magnitude of minimum translation speed accompany the changing locations at which this minimum forward motion occurs, reductions in the magnitude of minimum translation speed are minimal (Supplementary Fig. 5). This result is consistent with findings suggesting that slowdowns in TC minimum translation speed are not robust outside of the North Atlantic^{1,19,46,47}.

TC termination in and around Southeast Asia also varies as the planet warms. Changing termination points in the future indicate that some regions may see substantially amplified TC hazards compared to historical norms. For instance, an increase in TCs terminating over more inland regions (Fig. 5) suggests that storms persist longer over land (impacting more of mainland Southeast Asia). As another example, increases in TCs terminating along particularly northern or distant coastlines (such as Siberia, Alaska, and Canada; Supplementary Fig. 6) suggest these regions may be impacted by storms more frequently in a warmer future. Decreases in the probability of future TC termination in Japan, Southeast China, and the Philippines occur alongside increases in future TC termination over mainland Southeast Asia and inland China (Fig. 5). These shifts may be driven by future land-terminating TCs that persist longer than their historical counterparts after making their final landfall (Fig. 5G). Results from the Atlantic indicate that such a phenomenon may be driven by increased sea-surface temperatures, which allow storms to store more moisture capable of fueling TCs even when they are no longer located over water⁴⁸. The

Sixth Assessment Report of the Intergovernmental Panel on Climate Change suggests substantial future increases in sea-surface temperatures in the Northwest Pacific and other regions surrounding Southeast Asia that would support a similar mechanism driving the increasingly inland termination of future TCs in Southeast Asia⁴⁹. Future TCs also persist longer at more poleward latitudes than historical TCs, with storms becoming more likely to make landfall and terminate in areas like Siberia, Alaska, and western Canada (Supplementary Fig. 6). Such TC events may be particularly devastating, as illustrated in September 2022 when the remnants of Typhoon Merbok caused hurricane-strength winds and substantial coastal flooding along Alaskan coastlines⁵⁰.

The combined impacts of changes to TC genesis, intensification rates, minimum translation speeds, and termination have critical implications for coastal communities around Southeast Asia^{14,20,45,51}, including Hai Phong (Vietnam), Yangon (Myanmar), and Bangkok (Thailand). These cities constitute important population centers that are home to locations of societal, cultural, and economic significance^{52–55}.

Although TCs generally form closer to Southeast Asian coastlines in the future, there is minimal change in the time from when TCs form until they begin to impact these three cities in a warmer future (Supplementary Fig. 10), possibly due to a trade-off between genesis points that are located closer to coasts and reduced minimum translation speeds (Figs. 2 and 4). While this trade-off may prevent TCs from reaching Southeast Asian cities more quickly, other combinations of changing TC characteristics amplify potential impacts. For instance, the combination of faster TC intensification rates and a tendency for those fastest rates to occur near coastlines contributes to an increase in TC intensity at Hai Phong, Yangon, and Bangkok (Fig. 6A–E and Supplementary Fig. 9). All three locations also experience an increased duration of future TC impacts, likely due to slower-moving TCs in these regions (Fig. 6D–F). Though it is beyond the scope of this study, additional work that fully explores the interactions among changing TC characteristics to quantify the influence of each variation on TC hazards in these locations would be highly beneficial.

The combination of more intense, longer-lasting TCs at Hai Phong, Yangon, and Bangkok signals a greatly amplified TC hazard for Southeast Asia in a warming world. Furthermore, projected population growth around Hai Phong, Yangon, and Bangkok by the end of the twenty-first century suggests a future with significantly amplified exposure to these TC hazards. Both future scenarios considered here represent futures where coastal populations in Asia expand considerably relative to the year 2000 (~472 million)⁵⁶. With little management of coastal zone development, the moderate-emissions scenario (SSP2-4.5) is consistent with a future where coastal development continues similar to historical patterns, leading to additional urbanization and expanding cities⁵⁶. With rapid economic growth and heavy emphasis on international trade and tourism, the high-emissions scenario (SSP5-8.5) is consistent with a future where both urban and rural coastal populations expand significantly⁵⁶. By 2050, coastal populations in Asia are expected to expand to ~710 million under SSP2, and ~776 million under SSP5. By 2100, both scenarios see a slight decrease in coastal populations relative to mid-century to ~550 million, a value that nonetheless still exceeds present-day population⁵⁶.

As populations expand, major cities are often projected to grow particularly quickly. Hai Phong, a major port city for the Red River Delta, is

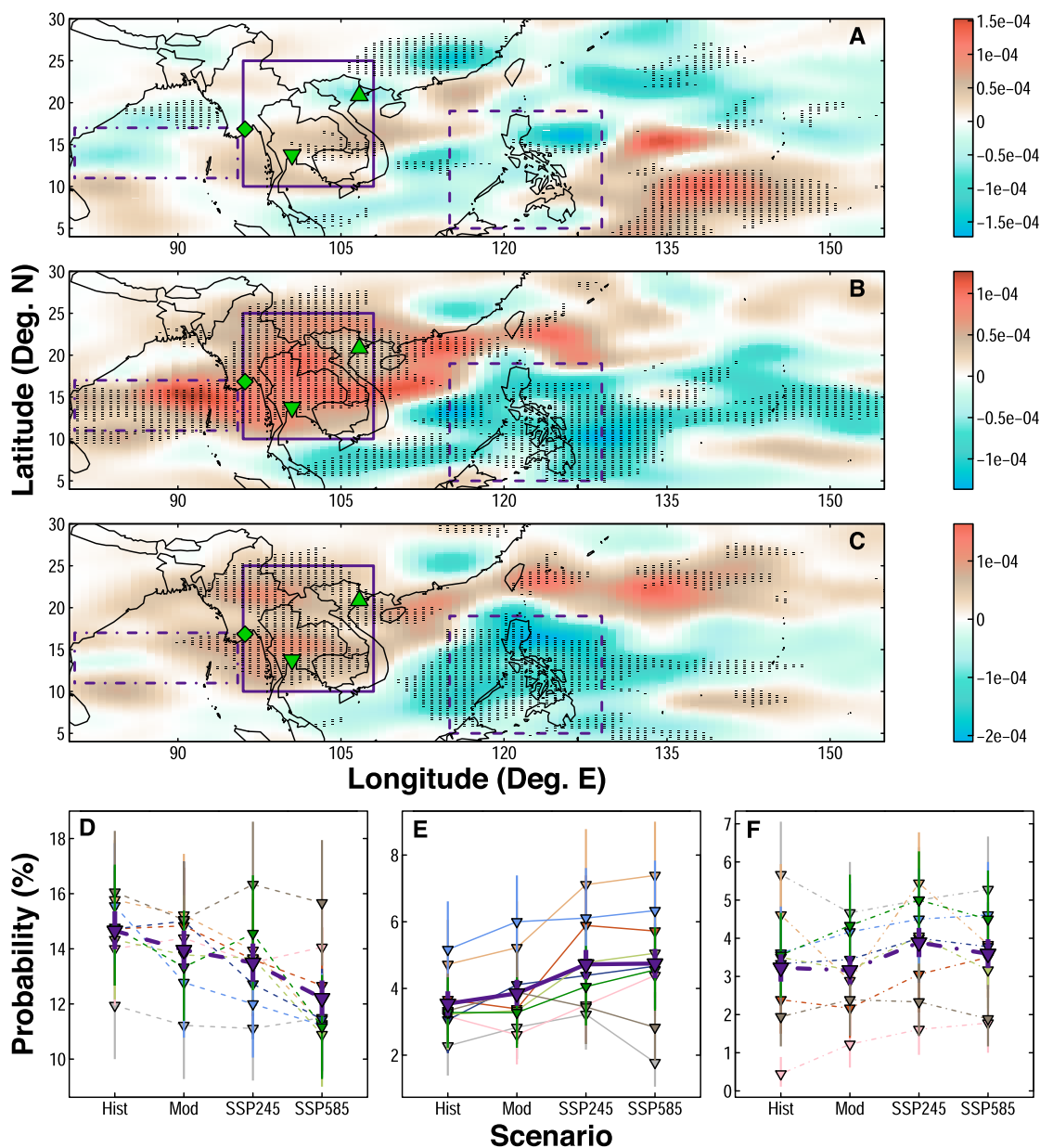


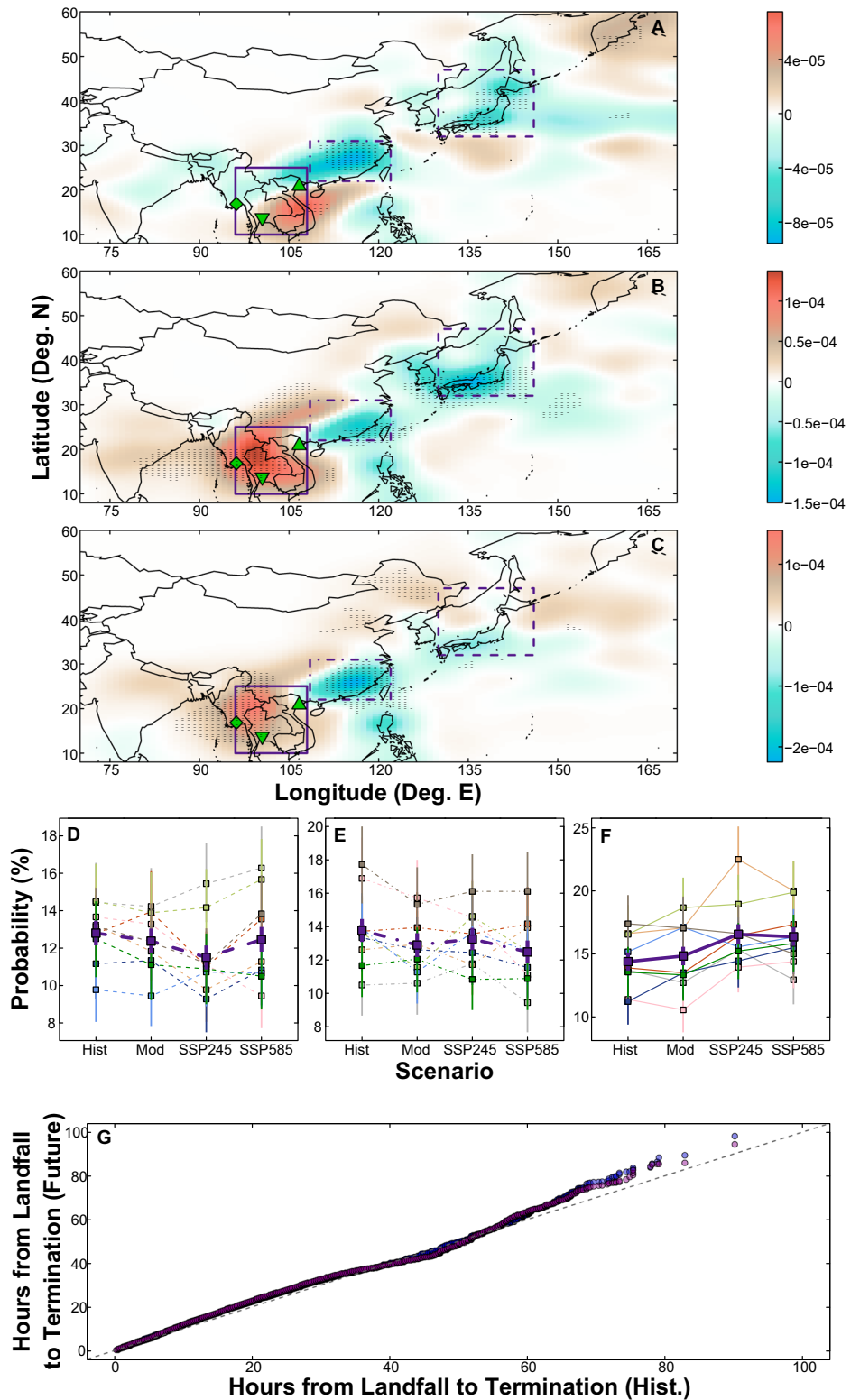
Fig. 4 | Density difference maps and probabilities of TC minimum translation speed points. Maps portraying the density differences in locations of TC minimum translation speeds for (A) the modern era (1981–2000) compared to the historical era (1881–1900), (B) a moderate-emissions future (2081–2100; SSP2-4.5) compared to the historical era, and (C) a high-emissions future (2081–2100; SSP5-8.5) compared to the historical era. Rectangles on the maps represent the Philippines region (dashed rectangle), the mainland Southeast Asia region (solid rectangle), and the Bay of Bengal region (dot-dash rectangle); green markers on maps indicate the locations of Hai Phong, Vietnam (upwards triangle); Bangkok, Thailand (downwards triangle); and Yangon, Myanmar (diamond). Hatching on maps shows grid cells where at least 7 of the 9 models assessed indicate the same sign (positive or negative) for

density difference. The density units shown by map color bars are track points per grid cell. Line plots indicate the probability of TCs reaching their minimum translation speed within the regions outlined by rectangles on the maps, including (D) the Philippines region, (E) the mainland Southeast Asia region, and (F) the Bay of Bengal region. Error bars on line plots show the bootstrapped 99% credible interval. Individual models shown in line plots are: CanESM (gray); CESM (pink); CNRM (orange); ECEarth (red); HadGEM (dark blue); IPSL (light green); MIROC (light blue); MPI (tan); and the UKESM (dark green). The ensemble mean is shown in purple. Note that y-axes in plots (D–F) are varied, to clearly show trends in each region.

located just ~100 km away from Vietnam’s capital of Hanoi. Also located in the Red River Delta, Hanoi’s population is anticipated to grow from ~4.7 million in 2010 to nearly 13 million by 2100⁵⁷. Similarly, Yangon’s population has been projected to increase from ~4.3 million in 2010 to nearly 11.5 million by 2100, and Bangkok’s population is projected to grow from ~6.9 million in 2010 to over 12 million by the end of the century⁵⁷. These population expansions suggest that nearly 2–3 times more people will be in the path of stronger and longer-lasting TCs by 2100, emphasizing the need for planning in the present to protect lives and economic assets in the future.

Many changes to TC tracks identified here are monotonic across time and emission scenarios; however, in some instances, there is a stronger signal for moderate emissions than high emissions. For example, in a moderate-emissions future compared to a high-emissions future, it is somewhat more likely for TCs to form and move most slowly in the Bay of Bengal, intensify most quickly in the South China Sea, and dissipate over mainland Southeast Asia (Figs. 2–5 and Table 1). In instances where results are nonmonotonic across emission scenarios, error bars for the model ensemble typically still overlap across emission scenarios, and the

Fig. 5 | Locations of TC termination. Maps portraying the density differences in TC termination for (A) the modern era (1981–2000) compared to the historical era (1881–1900), (B) a moderate emissions future (2081–2100; SSP2-4.5) compared to the historical era, and (C) a high emissions future (2081–2100; SSP5-8.5) compared to the historical era. Rectangles on the maps show the region around Japan (dashed rectangle), the Southeast Coast of China (dot-dash rectangle), and the mainland Southeast Asia region (solid rectangle); green markers on maps indicate the locations of Hai Phong, Vietnam (upwards triangle); Bangkok, Thailand (downwards triangle); and Yangon, Myanmar (diamond). Hatching on maps shows grid cells indicate the same sign (positive or negative) for density difference. The density units shown by map color bars are track points per grid cell. Line plots indicate the probability of TCs terminating within the regions outlined by rectangles on the maps, including (D) the Japan region, (E) the Southeast Chinese coast region, and (F) the mainland Southeast Asia region. Error bars on the line plots show the bootstrapped 99% credible interval. Individual models shown in line plots are: CanESM (gray); CESM (pink); CNRM (orange); ECEarth (red); HadGEM (dark blue); IPSL (light green); MIROC (light blue); MPI (tan); and the UKESM (dark green). The ensemble mean is shown in purple. Note that y-axes in plots (D–F) are varied, to clearly show trends in each region. G QQ plots of the length of time (in hours) for which land-terminating TCs persist after making their final landfall. QQ plots show the difference in quantiles of distributions from the historical era and a moderate-emissions future (blue), and the historical era and a high-emissions future (purple). Gray dashed lines on the QQ-plots show the one-to-one line; when points deviate from the line, the historical and future distributions are significantly different.

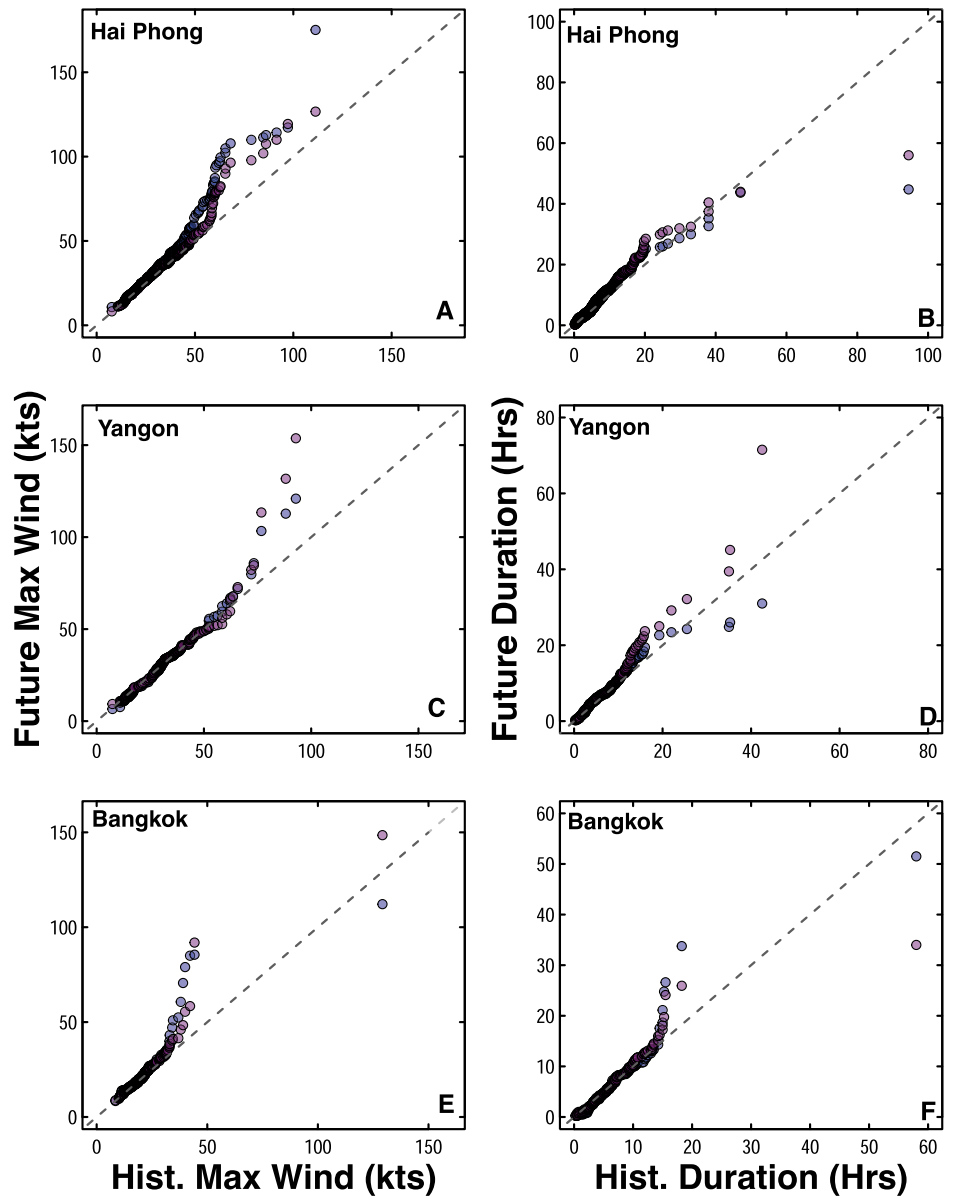


nonmonotonic behavior is usually strongly influenced by large variability across individual models.

Results pertaining to monotonic/nonmonotonic behavior of TC characteristics between emission scenarios for individual models are shown in Figs. 2–5, panels D–F. It is plausible that environmental variables from individual models, such as the simulation of the summer monsoon trough in each model (Supplementary Fig. 11 and Supplementary Table 1), and potential biases in El-Niño Southern Oscillation (ENSO) within each

model⁵⁸ (Supplementary Table 1), influence this behavior. Data is provided in Supplementary Table 1 alongside a monotonic score for each model for context, although these are only a subset of the potential environmental variables and biases in different models that could influence monotonic/nonmonotonic behavior in TC trajectory results. This highlights the substantial additional work that would be required by future studies to truly understand how modeled components and their interactions may affect monotonic/nonmonotonic TC behavior in future simulations.

Fig. 6 | Maximum wind speed and TC duration at points of interest. QQ plots showing the maximum wind speed reached (A, C, E) and duration (B, D, F) of TCs at (A, B) Hai Phong, Vietnam, (C, D) Yangon, Myanmar, and (E, F) Bangkok, Thailand. QQ plots show the difference in quantiles of distributions from the historical era and a moderate-emissions future (blue), and the historical era and a high-emissions future (purple). Gray dashed lines on the QQ plots show the one-to-one line; when points deviate from the line, the historical and future distributions are significantly different.



For example, additional influence on monotonic/nonmonotonic behavior may arise due to the contrasting effects of aerosols and greenhouse gases upon TC behavior⁵⁹. The SSP scenarios present a broader range of air-pollution pathways than past emissions scenarios, with lower concentrations of aerosols in the SSP2-4.5 scenario than in the SSP5-8.5 scenario⁶⁰⁻⁶². One recent study found that, particularly for decreased concentrations of aerosols that absorb radiation, Southeast Asia may see an increase in hydrologic sensitivity, amplifying warming effects upon precipitation⁶². Other studies have highlighted the fact that, especially in terms of intensity, aerosols are likely to impact TCs in an opposing manner to the effects of higher greenhouse gases upon TCs⁵⁹. This means that it is plausible that the impacts of aerosols in a high-emissions future may partially offset the expected impacts of increased emissions upon certain TC track characteristics, which may contribute to some of the nonlinearity observed across emissions scenarios within our results. As noted above, this highlights the need for additional studies to fully understand drivers of monotonic/non-monotonic behavior in future TC trajectory characteristics.

TCs are amongst the most damaging and costly natural hazards to impact coastal communities around the world^{89,63}, but are of particular concern in Southeast Asia due to the presence of low-lying, highly populated

coastal cities. Changes to TC genesis, intensification rates, minimum translation speeds, and termination in both moderate- and high-emissions futures suggest critical changes to TC tracks that will impact the hazard facing coastal communities in Southeast Asia by the end of the century, including potentially more intense and longer-lasting TCs at key coastal cities including Hai Phong, Bangkok, and Yangon. Changing hazards are furthermore not limited to coastal communities in a warmer future, as many land-terminating TCs persist longer after making landfall, with the potential to extend damage footprints farther inland. These results highlight not only a need to mitigate additional warming by rapidly cutting anthropogenic greenhouse emissions, but also a dire need for careful adaptation and planning in affected communities to minimize future damages and increase resiliency to TC hazards.

Methods

Tropical cyclone and CMIP6 data

We use synthetic TCs downscaled from nine CMIP6 global climate models (GCMs). The statistical/deterministic model used to generate TCs is described elsewhere (e.g., refs. 64–66). We produce large numbers of synthetic TCs (90 TCs from each model during each year in each period, or a

total of 16,200 TCs in each period) under a range of plausible past and future climate scenarios to understand how TC tracks may already have evolved from historical norms, and how future warming may further impact TC track behavior. Both thermodynamic and kinematic state variables from CMIP6 GCMs are used to create TC datasets⁶⁷.

A random seeding process is used to produce TCs for our synthetic datasets⁶⁵. For this method, warm-core vortices with maximum wind speeds of 12 m s^{-1} and minimal mid-level humidity anomalies are placed randomly at all locations poleward of 2° latitude and all parts of the year in basins relevant to TC impacts on Southeast Asia. Most seeds do not evolve into TCs, due to unfavorable environmental conditions for TC genesis, such as sub-optimal potential intensity or high wind shear. However, if the seeds evolve to have winds of at least 21 m s^{-1} (40 kts), they are considered a TC⁶⁵, and are added to the downscaled track datasets. The first 2-h time step after a seed that forms a TC is placed serves as the genesis point for the storm.

To simulate TC tracks, a beta-and-advection model is used, incorporating 850 hPa and 250 hPa wind variables from the CMIP6 GCMs to approximate TC motion⁶⁵. Past work comparing synthetic TC tracks from the observational era with observed TC tracks from the National Oceanic and Atmospheric Administration's HURDAT2 database in the Atlantic⁶⁸ shows good agreement between the patterns of TC tracks simulated with this approach and observed TC track behavior¹⁷. TC tracks are terminated either when TC maximum wind speeds are sufficiently diminished (below 13 m s^{-1}), or after the storm has existed for 30 days.

The nine CMIP6 models used to generate TCs for this work include CanESM (Canadian Earth System Model version 5)⁶⁹, CESM (Community Earth System Model version 2)⁷⁰, CNRM (Centre National de Recherches Meteorologiques and Cerfacs version 6-1)⁷¹, ECEarth (European Centre Earth System Model version 3)⁷², HadGEM (Hadley Centre Global Environment Model version 3)⁷³, IPSL (Institut Pierre-Simon Laplace Climate Model version 6)⁷⁴, MIROC (the Sixth Version of the Model for Interdisciplinary Research on Climate)⁷⁵, MPI (Max Planck Institute for Meteorology Earth System Model)⁷⁶, and the UK Model (United Kingdom Earth System Model version 1)⁷⁷. We choose these nine models since all include the necessary fields to downscale TC tracks in each period, and to ensure that our results are informed by a reasonably broad ensemble of CMIP models. TCs simulated from these models are filtered with the requirement that they travel either partially or entirely within a bounding box around Southeast Asia that extends from 10°S to 25°N , and from 90°E to 140°E . CMIP6 simulations from these nine models include all the necessary variables to downscale TCs for the historical, modern, and future (SSP2-4.5 and SSP5-8.5) eras, allowing our work to assess not only how TCs may change in various plausible future climates, but also to establish a historical context for those changes. The historical, modern, and future eras are defined as:

- Historical Era (1881–1900): a historical climate prior to the most dramatic impacts of anthropogenic greenhouse gas emissions.
- Modern Era (1981–2000): a climate similar to the recent observational era and current conditions.
- Moderate-Emissions Future (2081–2100): a “middle of the road” future climate in which slow but steady progress is made toward lowering anthropogenic greenhouse gas emissions, resulting in 4.5 W m^{-2} radiative forcing for the planet by the year 2100^{26,78}.
- High-Emissions Future (2081–2100): a future climate in which “fossil-fuel development” dominates energy-supply needs, and anthropogenic greenhouse gas emissions remain very high, resulting in 8.5 W m^{-2} radiative forcing for the planet by the year 2100^{26,78}.

As with any modeling study, uncertainty will unavoidably be introduced to our results based on the selection of CMIP6 models included in the downscaled ensemble (including mean-state biases^{79–82}, and responses to processes not fully investigated here, such as interannual to decadal climate variability under various SSPs, and uncertainty related to the ENSO state in the GCMs)^{80,83}. Because each model will also inevitably have unique biases related to the simulation of large-scale variables (such as mid-level humidity

anomalies and 850 hPa and 250 hPa winds)^{84,85} upon which our downscaling method depends, we have taken steps to ensure transparency within our results by showing results from individual models alongside the full model ensemble average for key regions (Figs. 2–5, panels D–F). We have also included more models in our ensemble than were used in similar studies for the Atlantic^{17,29}, lending additional confidence to the robustness of our results within the context of similar studies in the field. Finally, given the importance of the monsoon climate for TC activity in Southeast Asia, we have verified that, overall, our models can simulate the mean structure of the monsoon trough over the Indian subcontinent in June, July, and August relative to ERA5 reanalysis (Supplementary Fig. 11), which helps to instill confidence in this aspect of model simulation.

Additional uncertainty may arise from the downscaling process used to generate synthetic TC tracks for this study^{64,65,67}. For instance, given the importance of sea surface temperatures for the downscaling process^{64–66}, it is plausible that TC track simulation over land is more uncertain than for tracks that remain over water. Where possible, we have taken steps to minimize uncertainty associated with the downscaling process. For example, the downscaling process used here^{64–66} diverges from the majority of other recent studies by producing a future increase in TC frequency, rather than a decreased overall TC frequency with additional warming¹⁰. For this reason, we specifically focus on broad spatial variations and proportional changes in TC characteristics across key regions over time, rather than attempting to quantify explicit changes in TC occurrences or frequency. Because of limitations introduced by the selection of CMIP6 models and downscaling techniques, further studies of changing TC characteristics in this region that explore results from additional global climate models or downscaling methods would be highly beneficial.

An additional caveat specific to this study that should be noted is that because of the filtering process used for TC tracks, our results cover TC events in multiple basins, including the Northwest Pacific (where most of our tracks occur), the Southwestern Pacific Ocean, the Northern Indian Ocean, and the Southeastern Indian Ocean near Australia and Indonesia. Results, therefore, are not generally representative of changes within any one of these ocean basins as a whole, but are highly relevant for the subset of TCs that impact the densely populated Southeast Asian region. Furthermore, while this work focuses on broad variations across periods, additional research to consider seasonal variations in how such metrics evolve in a warmer climate may be warranted.

Statistical analyses

To compute density differences shown in Figs. 2–5 and Supplementary Figs. 1, 2, 4, and 6, kernel density estimates are computed for each era, and historical density estimates are subtracted from each of the other estimates. The density units shown by colorbars for these figures are track points per grid cell, and each map is constructed on a 100×100 grid. Map resolutions for plots in Figs. 2–4 are 0.75° longitude by 0.26° latitude; resolutions for plots in Fig. 5 are 1° longitude by 0.52° latitude. Supplementary figures cover broader regions and therefore have more coarse resolutions of up to 2.28° longitude by 1.42° latitude. It should be noted that maps are generated using the worldmap package in R, and that it is possible that the boundaries of countries displayed in the map may not always perfectly align with accepted political boundaries.

Probabilities of particular TC characteristics as illustrated in Figs. 2–5 and reported in non-colored text Table 1 are determined by finding the total of all TCs that meet a particular requirement in a particular era (i.e., all TCs with South China Sea genesis in the historical period) and putting that value in terms of a percentage for all TCs during that period (i.e., all TC genesis during the historical period). For example, if a total of 100 TCs were generated in the historical period, and 5 of those TCs formed in the South China Sea, the percentage of South China Sea genesis for the historical period would be 5%, and this would be the value shown on the line plots (Figs. 2–5) and in column 1 of Table 1.

Because the datasets used here include TCs for a variety of ocean basins across a relatively broad region, the overall percentages within specific

regions of focus are sometimes relatively small. For that reason, we also include analyses of the proportional change of TC characteristics within individual regions from one period to another. These proportional changes are not shown explicitly in Figs. 2–5, but are reported in square, color-coded brackets in the final two columns of Table 1. Proportional changes are calculated using the same approach as ref. 29, as illustrated in Eq. (1):

$$\frac{P_{\text{new}} - P_{\text{initial}}}{P_{\text{initial}}} \times 100\% \quad (1)$$

Where P_{initial} is the initial percentage of TCs with a certain characteristic (for instance, percentage of TC genesis in the South China Sea during the historical period), and P_{new} is the new percentage of TCs with a certain characteristic (for instance, percentage of TC genesis in the South China sea during a moderate-emissions future). Consider the example above, where we found 5% genesis for the South China Sea in the historical period. If that percentage increases to 8% in a moderate-emissions future, then we would say that there is a 60% proportional increase in South China Sea genesis in a moderate emissions future compared to the historical era, as shown below, in Eq. (2):

$$\frac{P_{\text{new}} - P_{\text{initial}}}{P_{\text{initial}}} \times 100\% \rightarrow \frac{8 - 5}{5} \times 100\% \rightarrow \frac{3}{5} \times 100\% = 60\% \quad (2)$$

Credible intervals discussed throughout the text and shown in Figs. 2–5, Supplementary Fig. 9 and Table 1 are determined by bootstrapping the original TC datasets. Bootstrapping refers to a process of resampling the original data n times with replacement, where n is the total number of bootstrap samples. The new samples are the same length as the original dataset and can be used to assess confidence ranges around the desired statistic^{86,87}. We construct 99% credible intervals using $n = 5000$ samples of each TC characteristic in Figs. 2–5 and Table 1. In Supplementary Fig. 9, we bootstrap the means of upper tails of max wind and duration at points of interest using $n = 5000$ samples to find the 66% and 90% credible intervals surrounding the mean of the tails.

Figures 5 and 6 and Supplementary Fig. 10 all include quantile-quantile plots, or QQ plots. QQ plots are developed by plotting the quantiles of two separate distributions against one another in a scatterplot. If the points representing the quantiles from the two distributions fall on a one-to-one line, the two distributions are considered statistically similar. However, if points representing the quantiles from the two distributions deviate from the one-to-one line, the distributions are considered statistically significantly different from one another. Dashed one-to-one lines are included on all QQ plots to provide a visual representation of the similarities and differences between the distributions being compared⁵³.

Locations of focus for QQ plots, probability density functions, and line plots in Fig. 6 and Supplementary Figs. 8–10 are chosen for their proximity to regions where the greatest changes in TC tracks occur (Figs. 2–5) as well as their cultural and economic significance to Southeast Asia and surrounding regions⁵³. Results pertaining to these points of interest (Hai Phong, Yangon, and Bangkok; Fig. 6 and Supplementary Figs. 8–10) indicate the changing TC hazard for those locations based on results from the broader TC tracks dataset, and should not be misinterpreted as a separate, finer, city-scale downscaling project. The duration of TC track impacts at each location for an individual TC track is found by calculating the length of time (hours) that the distance from the TC center to the point of interest is less than the TC's radius of maximum winds. In other words, the duration is the amount of time that the city remains within range of the TC's radius of maximum winds as the storm travels near the location. The TC maximum wind at each location is found by isolating the TC maximum wind speed while the city is within the TC's radius of maximum winds (i.e., while the TC impacts the location). This approach to assessing duration may result in conservative estimates for the length of TC impacts, since the city may also face exposure to more peripheral storm winds or other TC hazards beyond the radius of maximum wind. The time from storm formation until the TC reaches the city (Supplementary

Fig. 10) is calculated as the amount of time from when the TC forms until the time when the TC comes within 100 km of the city's latitude/longitude.

Data availability

This work uses simulated tropical cyclones downscaled from a model developed by Kerry Emanuel (Massachusetts Institute of Technology), and described in Emanuel et al.^{64–66}. All inputs to the tropical cyclone model come from CMIP6 datasets that are publicly available from the Earth System Grid Federation website (<https://esgf-node.llnl.gov/projects/cmip6/>). Downscaled fields from the tropical cyclone model, including storm tracks as defined by TC latitude and longitude at 2-h intervals, are available for research purposes from K. Emanuel (emanuel@mit.edu) on request. Researchers will be asked to sign a non-redistribution agreement and assert that the data will be used for nonprofit research only. Gridded population data are available from <https://sedac.ciesin.columbia.edu/data/set/gpw-v4-population-density-rev11/data-download>.

Code availability

This work uses code developed in R. The code can be found in an open access repository, here: <https://zenodo.org/records/11479378>.

Received: 20 February 2024; Accepted: 21 June 2024;

Published online: 02 July 2024

References

1. Seneviratne, S. I. et al. Weather and climate extreme events in a changing climate. in *Climate Change 2021: The Physical Science Basis. Contribution of Working Group I to the Sixth Assessment Report of the Intergovernmental Panel on Climate Change* (eds Masson-Delmotte, V. et al.) (Cambridge University Press, 2021).
2. Camargo, S. J. et al. Topic 6.3: tropical cyclones and climate change. in *Tenth International Workshop on Tropical Cyclones (IWTC-10)* (2022).
3. Stampe, J. et al. *Climate Change and Sovereign Risk* (SOAS University of London, Asian Development Bank Institute, World Wide Fund for Nature Singapore, 2020).
4. Gerstl, A. & Helmke, B. The Association of Southeast Asian Nations (ASEAN) and climate change: a threat to national, regime, and human security. in *Human Security: Securing East Asia's Future* (ed. Teh Cheng Guan, B.), Vol. 1 135–156 (Springer Netherlands, 2012).
5. Zhu, S. et al. Conspicuous temperature extremes over Southeast Asia: seasonal variations under 1.5 °C and 2 °C global warming. *Clim. Change* **160**, 343–360 (2020).
6. Ge, F. et al. Risks of precipitation extremes over Southeast Asia: does 1.5 °C or 2 °C global warming make a difference? *Environ. Res. Lett.* **14**, 044015 (2019).
7. Kulp, S. A. & Strauss, B. H. New elevation data triple estimates of global vulnerability to sea-level rise and coastal flooding. *Nat. Commun.* **10**, 1–12 (2019).
8. Cerverny, R. S. et al. WMO assessment of weather and climate mortality extremes: lightning, tropical cyclones, tornadoes, and hail. *Weather Clim. Soc.* **9**, 487–497 (2017).
9. Emanuel, K. Increasing destructiveness of tropical cyclones over the past 30 years. *Nature* **436**, 686–688 (2005).
10. Knutson, T. et al. Tropical cyclones and climate change assessment: part II. Projected response to anthropogenic warming. *Bull. Am. Meteorol. Soc.* **101**, 303–322 (2019).
11. Mei, W. & Xie, S. P. Intensification of landfalling typhoons over the northwest Pacific since the late 1970s. *Nat. Geosci.* **9**, 753–757 (2016).
12. Chen, J. et al. Changing impacts of tropical cyclones on East and Southeast Asian inland regions in the past and a globally warmed future climate. *Front. Earth Sci.* **9**, 1065 (2021).
13. Li, R. C. Y., Zhou, W., Shun, C. M. & Lee, T. C. Change in destructiveness of landfalling tropical cyclones over China in recent decades. *J. Clim.* **30**, 3367–3379 (2017).

14. Tran, T. L., Ritchie, E. A., Perkins-Kirkpatrick, S. E., Bui, H. & Luong, T. M. Future changes in tropical cyclone exposure and impacts in Southeast Asia from CMIP6 pseudo-global warming simulations. *Earths Future* **10**, e2022EF003118 (2022).
15. Liu, K. S. & Chan, J. C. L. Growing threat of rapidly-intensifying tropical cyclones in East Asia. *Adv. Atmos. Sci.* **39**, 222–234 (2022).
16. Emanuel, K. The dependence of hurricane intensity on climate. *Nature* **326**, 483–485 (1987).
17. Garner, A. J., Kopp, R. E. & Horton, B. P. Evolving tropical cyclone tracks in the North Atlantic in a warming climate. *Earths Future* **9**, e2021EF002326 (2021).
18. Studholme, J., Fedorov, A. V., Gulev, S. K., Emanuel, K. & Hodges, K. Poleward expansion of tropical cyclone latitudes in warming climates. *Nat. Geosci.* **15**, 14–28 (2021).
19. Kossin, J. P. A global slowdown of tropical-cyclone translation speed. *Nature* **558**, 104–107 (2018).
20. Tran, T. L., Ritchie, E. A. & Perkins-Kirkpatrick, S. E. A 50-year tropical cyclone exposure climatology in Southeast Asia. *J. Geophys. Res. Atmos.* **127**, e2021JD036301 (2022).
21. Kossin, J. P., Emanuel, K. A. & Camargo, S. J. Past and projected changes in western north pacific tropical cyclone exposure. *J. Clim.* **29**, 5725–5739 (2016).
22. Nakamura, J. et al. Western North Pacific tropical cyclone model tracks in present and future climates. *J. Geophys. Res. Atmos.* **122**, 9721–9744 (2017).
23. Lee, M. et al. Long-term trends in tropical cyclone tracks around Korea and Japan in late summer and early fall. *Atmos. Sci. Lett.* **20**, e939 (2019).
24. Hirano, A. Effects of climate change on spatiotemporal patterns of tropical cyclone tracks and their implications for coastal agriculture in Myanmar. *Paddy Water Environ.* **19**, 261–269 (2021).
25. Eyring, V. et al. Overview of the Coupled Model Intercomparison Project Phase 6 (CMIP6) experimental design and organisation. *Geosci. Model Dev. Discuss.* **8**, 10539–10583 (2015).
26. Meinshausen, M. et al. The shared socio-economic pathway (SSP) greenhouse gas concentrations and their extensions to 2500. *Geosci. Model Dev.* **13**, 3571–3605 (2020).
27. Sharmila, S. & Walsh, K. J. E. Recent poleward shift of tropical cyclone formation linked to Hadley cell expansion. *Nat. Clim. Change* **8**, 730–736 (2018).
28. Daloz, A. S. & Camargo, S. J. Is the poleward migration of tropical cyclone maximum intensity associated with a poleward migration of tropical cyclone genesis? *Clim. Dyn.* **50**, 705–715 (2018).
29. Weaver, M. M. & Garner, A. J. Varying genesis and landfall locations for North Atlantic tropical cyclones in a warmer climate. *Sci. Rep.* **13**, 1–14 (2023).
30. Park, D. S. R., Ho, C. H. & Kim, J. H. Growing threat of intense tropical cyclones to East Asia over the period 1977–2010. *Environ. Res. Lett.* **9**, 014008 (2014).
31. Bhaskar Rao, D. V., Srinivas, D. & Satyanarayana, G. C. Trends in the genesis and landfall locations of tropical cyclones over the Bay of Bengal in the current global warming era. *J. Earth Syst. Sci.* **128**, 1–10 (2019).
32. Deshpande, M. et al. Changing status of tropical cyclones over the north Indian Ocean. *Clim. Dyn.* **57**, 3545–3567 (2021).
33. Kossin, J. P., Emanuel, K. A. & Vecchi, G. A. The poleward migration of the location of tropical cyclone maximum intensity. *Nature* **509**, 349–352 (2014).
34. Lucas, C., Timbal, B. & Nguyen, H. The expanding tropics: a critical assessment of the observational and modeling studies. *Wiley Interdiscip. Rev. Clim. Change* **5**, 89–112 (2013).
35. Garner, A. J. Observed increases in North Atlantic tropical cyclone peak intensification rates. *Sci. Rep.* **13**, 1–12 (2023).
36. Li, Y. et al. Recent increases in tropical cyclone rapid intensification events in global offshore regions. *Nat. Commun.* **14**, 1–9 (2023).
37. Emanuel, K. Will global warming make hurricane forecasting more difficult? *Bull. Am. Meteorol. Soc.* **98**, 495–501 (2017).
38. Lai, Y. et al. Greater flood risks in response to slowdown of tropical cyclones over the coast of China. *Proc. Natl Acad. Sci. USA* **117**, 14751–14755 (2020).
39. Kemp, A. C. & Horton, B. P. Contribution of relative sea-level rise to historical hurricane flooding in New York City. *J. Quat. Sci.* **28**, 537–541 (2013).
40. Reed, A. J. et al. Increased threat of tropical cyclones and coastal flooding to New York City during the anthropogenic era. *Proc. Natl Acad. Sci.* **112**, 12610–12615 (2015).
41. Jalad, R. *Sitrep No. 29 Re Preparedness Measures and Effects for Typhoon 'ULYSSES' (I.N. VAMCO)*. (2021).
42. Kurata, Y. B., Prasetyo, Y. T., Ong, A. K. S., Nadlifatin, R. & Chuenyindee, T. Factors affecting perceived effectiveness of Typhoon Vamco (Ulysses) flood disaster response among Filipinos in Luzon, Philippines: an integration of protection motivation theory and extended theory of planned behavior. *Int. J. Disaster Risk Reduct.* **67**, 102670 (2022).
43. Jyoteeshkumar Reddy, P., Sriram, D., Gunthe, S. S. & Balaji, C. Impact of climate change on intense Bay of Bengal tropical cyclones of the post-monsoon season: a pseudo global warming approach. *Clim. Dyn.* **56**, 2855–2879 (2021).
44. Chu, P. S., Kim, J. H. & Ruan Chen, Y. Have steering flows in the western North Pacific and the South China Sea changed over the last 50 years? *Geophys. Res. Lett.* **39**, 10704 (2012).
45. Chen, A., Giese, M. & Chen, D. Flood impact on Mainland Southeast Asia between 1985 and 2018—the role of tropical cyclones. *J. Flood Risk Manag* **13**, e12598 (2020).
46. Zhang, D. et al. Changes in tropical-cyclone translation speed over the Western North Pacific. *Atmosphere* **11**, 93 (2020).
47. Yamaguchi, M. & Maeda, S. Slowdown of typhoon translation speeds in mid-latitudes in September influenced by the Pacific decadal oscillation and global warming. *J. Meteorol. Soc. Jpn. Ser. II* **98**, 1321–1334 (2020).
48. Li, L. & Chakraborty, P. Slower decay of landfalling hurricanes in a warming world. *Nature* **587**, 230–234 (2020).
49. Fox-Kemper, B. et al. Ocean, cryosphere and sea level change. in *Climate Change 2021: The Physical Science Basis. Contribution of Working Group I to the Sixth Assessment Report of the Intergovernmental Panel on Climate Change* (eds Masson-Delmotte, V. et al.) (Cambridge University Press, 2021).
50. NOAA National Centers for Environmental Information. *Annual 2022 Tropical Cyclones Report*. (National Oceanic and Atmospheric Administration, 2022).
51. Takahashi, H. G. Long-term changes in rainfall and tropical cyclone activity over South and Southeast Asia. *Adv. Geosci.* **30**, 17–22 (2011).
52. Sritarapat, T. & Takeuchi, W. Urban growth modeling based on the multi-centers of the urban areas and land cover change in Yangon, Myanmar. *J. Remote Sens. Soc. Jpn.* **37**, 248–260 (2017).
53. Kraas, F. Megacities and global change in East, Southeast and South Asia. *Ger. J. Contemp. Asia* **103**, 9–22 (2021).
54. Choomgrant, K. & Sukharomana, R. A vibrant life by the Chao Phraya River, Northern Bangkok Thailand: the heritage tourism value of Baan Lao community. in *Proceedings of the 2017 International Conference on Economics, Finance and Statistics (ICEFS 2017)* 26, 168–176 (2017).
55. Nguyen, T. D. Marine economic development: a case study of Hai Phong, Vietnam. *J. Int. Bus. Manag.* **5**, 01–11 (2022).
56. Merkens, J. L., Reimann, L., Hinkel, J. & Vafeidis, A. T. Gridded population projections for the coastal zone under the shared socioeconomic pathways. *Glob. Planet Change* **145**, 57–66 (2016).
57. Hoornweg, D. & Pope, K. Population predictions for the world's largest cities in the 21st century. *Environ. Urban* **29**, 195–216 (2017).

58. Erickson, N. E. & Patricola, C. M. Future projections of the El Niño–Southern oscillation and tropical Pacific mean state in CMIP6. *J. Geophys. Res. Atmos.* **128**, e2022JD037563 (2023).
59. Wang, Y., Lee, K. H., Lin, Y., Levy, M. & Zhang, R. Distinct effects of anthropogenic aerosols on tropical cyclones. *Nat. Clim. Change* **4**, 368–373 (2014).
60. Lund, M. T., Myhre, G. & Samset, B. H. Anthropogenic aerosol forcing under the shared socioeconomic pathways. *Atmos. Chem. Phys.* **19**, 13827–13839 (2019).
61. Turnock, S. T. et al. Historical and future changes in air pollutants from CMIP6 models. *Atmos. Chem. Phys.* **20**, 14547–14579 (2020).
62. McCoy, I. L., Vogt, M. A. & Wood, R. Absorbing aerosol choices influences precipitation changes across future scenarios. *Geophys. Res. Lett.* **49**, e2022GL097717 (2022).
63. Rappaport, E. N. Fatalities in the United States from Atlantic tropical cyclones: new data and interpretation. *Bull. Am. Meteorol. Soc.* **95**, 341–346 (2014).
64. Emanuel, K., Ravela, S., Vivant, E. & Risi, C. A statistical deterministic approach to hurricane risk assessment. *Bull. Am. Meteorol. Soc.* **87**, 299–314 (2006).
65. Emanuel, K., Sundararajan, R. & Williams, J. Hurricanes and global warming: results from downscaling IPCC AR4 simulations. *Bull. Am. Meteorol. Soc.* **89**, 347–367 (2008).
66. Emanuel, K. Response of global tropical cyclone activity to increasing CO₂: results from downscaling CMIP6 models. *J. Clim.* **34**, 57–70 (2021).
67. O’Neill, B. C. et al. The Scenario Model Intercomparison Project (ScenarioMIP) for CMIP6. *Geosci. Model Dev.* **9**, 3461–3482 (2016).
68. Landsea, C. W. & Franklin, J. L. Atlantic hurricane database uncertainty and presentation of a new database format. *Mon. Weather Rev.* **141**, 3576–3592 (2013).
69. Swart, N. C. et al. The Canadian Earth System Model version 5 (CanESM5.0.3). *Geosci. Model Dev.* **12**, 4823–4873 (2019).
70. Danabasoglu, G. et al. The Community Earth System Model Version 2 (CESM2). *J. Adv. Model Earth Syst.* **12**, e2019MS001916 (2020).
71. Voldoire, A. et al. Evaluation of CMIP6 DECK experiments with CNRM-CM6-1. *J. Adv. Model Earth Syst.* **11**, 2177–2213 (2019).
72. Döscher, R. et al. The EC-Earth3 earth system model for the Coupled Model Intercomparison Project 6. *Geosci. Model Dev.* **15**, 2973–3020 (2022).
73. Andrews, M. B. et al. Historical simulations with HadGEM3-GC3.1 for CMIP6. *J. Adv. Model Earth Syst.* **12**, e2019MS001995 (2020).
74. Lurton, T. et al. Implementation of the CMIP6 forcing data in the IPSL-CM6A-LR model. *J. Adv. Model Earth Syst.* **12**, e2019MS001940 (2020).
75. Tatebe, H. et al. Description and basic evaluation of simulated mean state, internal variability, and climate sensitivity in MIROC6. *Geosci. Model Dev.* **12**, 2727–2765 (2019).
76. Gutjahr, O. et al. Max Planck Institute Earth System Model (MPI-ESM1.2) for the High-Resolution Model Intercomparison Project (HighResMIP). *Geosci. Model Dev.* **12**, 3241–3281 (2019).
77. Senior, C. A. et al. U.K. community Earth system modeling for CMIP6. *J. Adv. Model Earth Syst.* **12**, e2019MS002004 (2020).
78. van Vuuren, D. P. et al. The representative concentration pathways: an overview. *Clim. Change* **109**, 5–31 (2011).
79. Raavi, P. H. & Walsh, K. J. E. Sensitivity of tropical cyclone formation to resolution-dependent and independent tracking schemes in high-resolution climate model simulations. *Earth Space Sci.* **7**, e2019EA000906 (2020).
80. Sobel, A. H. et al. Near-term tropical cyclone risk and coupled Earth system model biases. *Proc. Natl Acad. Sci. USA* **120**, e2209631120 (2023).
81. Samanta, D. et al. Coupled model biases breed spurious low-frequency variability in the tropical Pacific Ocean. *Geophys. Res. Lett.* **45**, 10,609–10,618 (2018).
82. Samanta, D. et al. Impact of a narrow coastal Bay of Bengal sea surface temperature front on an Indian summer monsoon simulation. *Sci. Rep.* **8**, 1–12 (2018).
83. Shan, K., Chu, P. S. & Yu, X. Interdecadal change of tropical cyclone translation speed during peak season in South China sea: observed evidence, model results, and possible mechanism. *J. Clim.* **36**, 4531–4541 (2023).
84. Han, Y., Zhang, M. Z., Xu, Z. & Guo, W. Assessing the performance of 33 CMIP6 models in simulating the large-scale environmental fields of tropical cyclones. *Clim. Dyn.* **58**, 1683–1698 (2022).
85. Sainsbury, E. M. et al. Can low-resolution CMIP6 ScenarioMIP models provide insight into future European post-tropical-cyclone risk? *Weather Clim. Dyn.* **3**, 1359–1379 (2022).
86. Efron, B. & Tibshirani, R. J. *An Introduction to the Bootstrap* (Chapman and Hall, 1993).
87. Efron, B. Bootstrap methods: another look at the jackknife. *Ann. Stat.* **7**, 1–26 (1979).

Acknowledgements

The authors wish to thank Kerry Emanuel (Massachusetts Institute of Technology) for the generation and use of synthetic TC datasets for this analysis. This research/project is supported by the Ministry of Education, Singapore, under its MOE Academic Research Fund #021940-00001 and Tier 3, Award MOE-MOET32022-0006. This is Earth Observatory of Singapore contribution number 574.

Author contributions

A.J.G., D.S., M.M.W., and B.P.H. all contributed to writing of the main text. A.J.G. and D.S. worked collaboratively to design the research. A.J.G. performed analyses and generated figures and tables for the study, except Fig. 1 and Supplementary Fig. 11, which D.S. produced.

Competing interests

The authors declare no competing interests.

Additional information

Supplementary information The online version contains supplementary material available at <https://doi.org/10.1038/s41612-024-00707-0>.

Correspondence and requests for materials should be addressed to Andra J. Garner.

Reprints and permissions information is available at <http://www.nature.com/reprints>

Publisher’s note Springer Nature remains neutral with regard to jurisdictional claims in published maps and institutional affiliations.

Open Access This article is licensed under a Creative Commons Attribution 4.0 International License, which permits use, sharing, adaptation, distribution and reproduction in any medium or format, as long as you give appropriate credit to the original author(s) and the source, provide a link to the Creative Commons licence, and indicate if changes were made. The images or other third party material in this article are included in the article’s Creative Commons licence, unless indicated otherwise in a credit line to the material. If material is not included in the article’s Creative Commons licence and your intended use is not permitted by statutory regulation or exceeds the permitted use, you will need to obtain permission directly from the copyright holder. To view a copy of this licence, visit <http://creativecommons.org/licenses/by/4.0/>.

© The Author(s) 2024